The clustering of the SDSS-IV extended Baryon Oscillation Spectroscopic Survey DR14 quasar sample: a tomographic measurement of cosmic structure growth and expansion rate based on optimal redshift weights

Gong-Bo Zhao [1,2,3]★ Yuting Wang,[1] Shun Saito,[4] Héctor Gil-Marín,[5,6] Will J. Percival,[3] Dandan Wang,[1,2] Chia-Hsun Chuang,[7,8] Rossana Ruggeri,[3] Eva-Maria Mueller,[3] Fangzhou Zhu,[9] Ashley J. Ross [3,10] Rita Tojeiro,[11] Isabelle Pâris,[12] Adam D. Myers,[13] Jeremy L. Tinker,[14] Jian Li,[1,2] Etienne Burtin,[15] Pauline Zarrouk,[15] Florian Beutler [3,16] Falk Baumgarten,[7,17] Julian E. Bautista,[18] Joel R. Brownstein [18] Kyle S. Dawson,[18] Jiamin Hou,[19,20] Axel de la Macorra,[21] Graziano Rossi,[22] John A. Peacock [23] Ariel G. Sánchez,[20] Arman Shafieloo [24,25] Donald P. Schneider[26,27] and Cheng Zhao [1,28]

Affiliations are listed at the end of the paper

ABSTRACT

We develop a new method, which is based on the optimal redshift weighting scheme, to extract the maximal tomographic information of baryonic acoustic oscillations (BAO) and redshift space distortions (RSD) from the extended Baryon Oscillation Spectroscopic Survey (eBOSS) Data Release 14 quasar (DR14Q) survey. We validate our method using the Extended Zel'dovich mocks, and apply our pipeline to the eBOSS DR14Q sample in the redshift range of $0.8 < z < 2.2$. We report a joint measurement of $f\sigma_8$ and two-dimensional BAO parameters D_A and H at four effective redshifts of $z_{\rm eff} = 0.98$, 1.23, 1.52, and 1.94, and provide the full data covariance matrix. Using our measurement combined with BOSS DR12, Main Galaxy Sample (MGS), and 6 degree Field Galaxy Survey (6dFGS) BAO measurements, we find that the existence of dark energy is supported by observations at a 7.4σ significance level. Combining our measurement with BOSS DR12 and *Planck* observations, we constrain the gravitational growth index to be $\gamma = 0.580 \pm 0.082$, which is fully consistent with the prediction of general relativity. This paper is part of a set that analyses the eBOSS DR14 quasar sample.

Key words: cosmological parameters – dark energy – distance scale – large-scale structure of Universe.

1 INTRODUCTION

In this era of precision cosmology, large spectroscopic galaxy surveys are one of the key probes of both the expansion history and structure growth of the Universe. Probing deep into the Universe, these surveys are able to provide rich information on the past light-cone, which is crucial to unveil the physics of the cosmic acceleration (Riess et al. 1998; Perlmutter et al. 1999), through studies of dark energy (Weinberg et al. 2013) and gravity on cosmological scales (Koyama 2016).

Baryonic acoustic oscillations (BAO) and redshift space distortions (RSD) are distinct three-dimensional clustering patterns probed by galaxy surveys, which are key to map the expansion history and the structure growth of the Universe respectively. Since a first successful measurement of BAO in 2005 (Eisenstein et al. 2005) and RSD in 2001 (Peacock et al. 2001), measurements with higher precision have been performing actively using large galaxy surveys (Percival et al. 2010; Beutler et al. 2011, 2012; Contreras et al. 2013; Kazin et al. 2014; Ross et al. 2015; The Dark Energy Survey Collaboration et al. 2017; Alam et al. 2017; Bautista et al. 2018; Ata et al. 2018).

Traditional BAO and RSD measurements are usually performed in a single, or a small number of redshifts slices, which is to guar-

★ E-mail: gbzhao@nao.cas.cn

antee that there are sufficiently large number of galaxies for the analysis to avoid large statistical or systematic uncertainties. However, this approach may give rise to information loss of the temporal evolution of the BAO or RSD signal, which is essential for tests of cosmological models. One solution to this problem is to perform BAO and RSD analyses in a large number of overlapping redshift slices to balance the level of uncertainty for the BAO/RSD analysis and the tomographic information (Zhao et al. 2017b; Wang et al. 2018b, 2017). However, this method is computationally expensive as it requires repetitive measurements and analysis with the computational cost scaling with $N_z(N_z - 1)/2$, where N_z is the number of redshift slices.

The optimal redshift weighting scheme, which was first developed for cosmological implications by Tegmark, Taylor & Heavens (1997), is a computationally efficient alternative. By designing the optimal redshift weights for a given set of parameters, one can in principle extract the light-cone information by fewer than N_p measurements, where N_p is the number of parameters to be measured. Given that N_p is usually a small number for BAO and RSD analyses, this approach significantly reduces the computational cost.

The optimal redshift method has been applied to BAO measurements in configuration space (Zhu, Padmanabhan & White 2015; Zhu et al. 2016, 2018), and RSD measurements in Fourier space (Ruggeri et al. 2017, 2018). In this work, we develop an alternative approach to Ruggeri et al. (2017, 2018) for a joint measurement of BAO and RSD in Fourier space, and apply our method to the extended Baryon Oscillation Spectroscopic Survey (eBOSS) Data Release 14 quasar (DR14Q) sample, followed by a cosmological implication.

The paper is structured as follows. In Section 2, we describe the observational and simulated data sets used in this analysis, and in Section 3, we present the method, followed by mock tests and main result of this work in Section 4. We compare our BAO and RSD measurements to the DR14Q companion papers presented in Section 5, followed by a cosmological implication of our measurement in Section 6, before conclusion and discussion in Section 7.

2 THE DATA SETS

In this section, we briefly describe the observational and simulated data sets used in this analysis. We refer the readers to a more detailed description of the DR14Q data sets in a companion paper of Gil-Marín et al. (2018).

2.1 The eBOSS DR14Q sample

Being part of the Sloan Digital Sky Survey-IV (SDSS-IV) project (Blanton et al. 2017), the eBOSS quasar survey (Dawson et al. 2016; Zhao et al. 2016) started in 2014 using a 2.5-m Sloan telescope (Gunn et al. 2006) at the Apache Point Observatory in New Mexico in the United States. After the eBOSS quasar target selection, which is described in Myers et al. (2015), the spectra are taken using the double-armed spectrographs (Smee et al. 2013), which were used for the BOSS mission, as part of the SDSS-III project (Eisenstein et al. 2011).

The data catalogue used in this analysis is the eBOSS quasar sample (Pâris et al. 2017), which is a part of the SDSS-IV DR14 (Abolfathi et al. 2018). This DR14Q catalogue consists of around 150 000 quasars with secure redshifts distributed across an effective area of 2112.9 deg² (see fig. 3 in a companion paper Gil-Marín et al. 2018 for a footprint of the DR14Q sample). A histogram for the redshift distribution for the quasar sample is shown in Fig. 1. Each
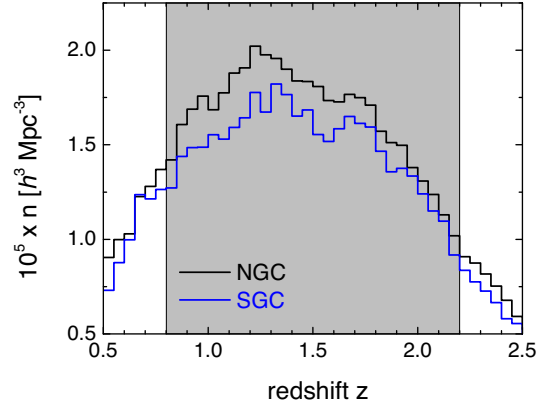
Figure 1. The observed volume number density (binned with $\Delta z = 0.05$) of the quasars in unit of h^3 Mpc^{-3} (multiplied by 10^5) as a function of redshifts in the NGC (upper black) and SGC (lower blue). The grey shaded region ($0.8 < z < 2.2$) shows the redshift range in which data are selected for this analysis.

quasar is given a total weight of

$$w_{tot} = w_{FKP} \; w_{sys} \; w_{spec} \sqrt{w_z}. \tag{1}$$

where w_{FKP}, w_{sys}, and w_{spec} denotes for the Feldman–Kaiser–Peacock (FKP) weight (Feldman, Kaiser & Peacock 1994), systematics weight, and the spectrum weight. The FKP weight is used to minimize the uncertainty of the power spectrum measurement, and w_{sys} corrects for the systematic effects from observing conditions including seeing, airmass, extinction, sky background, and so on (Ata et al. 2018). The spectrum weight accounts for the fibre collision and redshift failures (Gil-Marín et al. 2018; Zarrouk et al. 2018). In addition, we apply a redshift weight to each quasar to capture the tomographic information in redshift, which is detailed in Section 3.6.[1] The DR14Q sample used in this analysis is publicly available on the SDSS website https://data.sdss.org/sas/dr14/eboss/lss/catalogs/

2.2 The simulated mock samples

A large number of mock samples, each of which has the same clustering property of the eBOSS DR14Q sample, are required to estimate the data covariance matrix. In this analysis, we use the Extended Zel'dovich (EZ) mocks, which consist of 1000 realizations, produced following the prescription in Chuang et al. (2015). The cosmological parameters used for the EZ mocks are listed in equation (2), where the parameters are: the physical energy density of cold dark matter (CDM) and baryons, the sum of neutrino masses, the amplitude of the linear matter power spectrum within $8h^{-1}$ Mpc, the power index of the primordial power spectrum, and the (derived) scale of the sound horizon at recombination respectively.

$$\Theta \equiv \left\{ \Omega_c h^2, \Omega_b h^2, \sum M_\nu/eV, \sigma_8, n_s, r_d/Mpc \right\}$$
$$= \{0.1189, 0.0221, 0, 0.8225, 0.96, 147.66\}|_{EZ} \tag{2}$$

$$= \{0.1190, 0.022, 0.06, 0.8, 0.97, 147.78\}|_f \tag{3}$$

---

[1]As the redshift weights derived in Section 3.6 are for power spectrum multipoles, each quasar should be assigned a square root of the weights.

We list another set of parameters in equation (3), which is the fiducial cosmology we adopt for this analysis.[2]

Note that the EZ mocks used in this analysis include the full information on the light-cone, which is essential for the tomographic analysis in this study. The light-cone mocks were constructed by stacking simulation boxes at various redshifts. In order to match the time evolution of the clustering signal of the DR14Q sample, parameters used for the mocks were calibrated from the DR14Q sample in overlapping redshift slices, which is necessary to reduce the noise. For more details of the production of light-cone mocks, please refer to section 5.1 of Ata et al. (2018).

3 METHODOLOGY

In this section, we present details of the method used for this analysis, including the parametrization, the derivation of the optimal redshift weights, the template, and the likelihood analysis with details on parameter estimation.

We start by parametrizing the light-cone information of redshift surveys using a small number of parameters, and aim to derive a set of redshift weights to optimize the measurement of these parameters simultaneously.

3.1 Parametrizing tomographic information in redshift surveys

3.1.1 Parametrization of the BAO parameters

As in Zhu et al. (2015, 2016), we parametrize the redshift dependence of the transverse and radial dilations of the BAO distances $\alpha_\perp$ and $\alpha_\parallel$ using the following form,

$$
\alpha_\perp(z) \equiv \frac{D_A(z)}{D_A^f(z)}\theta = \alpha_0\left(1 + \alpha_1 x\right),
$$
$$
\alpha_\parallel(z) \equiv \frac{H_f(z)}{H(z)}\theta = \alpha_0\left(1 + \alpha_1 + 2\alpha_1 x\right),
$$
$$
x \equiv \chi_f(z)/\chi_f(z_p) - 1, \ \theta \equiv r_d^f/r_d, \tag{4}
$$

where χ is the comoving distance, and α_0 and α_1 are free parameters. This parametrization is essentially a Taylor expansion, and as stated in Zhu et al. (2015), it can well approximate the background expansion history of a wide range of cosmologies. The pivot redshift z_p is taken to be the effective redshift of the DR14Q sample, which is defined as follows (Samushia et al. 2014),

$$
z_p = z_{eff} = \frac{\sum_i z_i w_i^2}{\sum_i w_i^2}. \tag{5}
$$

Here w_i is the total weight of the ith data sample shown in equation (1). Note that in equation (4), x vanishes at $z = z_p$, which relates α_0 and α_1 to $\alpha_\perp(z_p)$ and $\alpha_\parallel(z_p)$ via,

$$
\alpha_\perp(z_p) = \alpha_0,
$$
$$
\alpha_\parallel(z_p) = \alpha_0\left(1 + \alpha_1\right). \tag{6}
$$

Plugging equation (6) into equation (4), one obtains,

$$
\alpha_\perp(z) = \alpha_\perp(z_p) + \left[\alpha_\parallel(z_p) - \alpha_\perp(z_p)\right] x,
$$
$$
\alpha_\parallel(z) = \alpha_\parallel(z_p) + 2\left[\alpha_\parallel(z_p) - \alpha_\perp(z_p)\right] x. \tag{7}
$$

[2]Throughout the paper, the subscript or superscript 'f' denotes the fiducial value.

3.1.2 Parametrization of the RSD parameters

We assume that the logarithmic growth rate f takes the form of (Linder 2005),

$$
f(z) \equiv \frac{\mathrm{dlog}\delta}{\mathrm{dlog}a} = [\Omega_M(z)]^\gamma = \left[\Omega_M H_0^2(1+z)^3\right]^\gamma \left[\frac{\alpha_\parallel(z)}{H_f(z)\theta}\right]^{2\gamma} \tag{8}
$$

where δ is the overdensity. With $f(z)|_{z=z_p} = f(z_p)$, the above equation can be recast into,

$$
f(z) = f(z_p)\left[\frac{\Omega_M(z)}{\Omega_M(z_p)}\right]^\gamma \tag{9}
$$

where

$$
\frac{\Omega_M(z)}{\Omega_M(z_p)} = \left(\frac{1+z}{1+z_p}\right)^3 \left[\frac{\alpha_\parallel(z)}{\alpha_\parallel(z_p)}\right]^2 \left[\frac{H_f(z_p)}{H_f(z)}\right]^2 \tag{10}
$$

$$
H_f(z) \propto \left[\Omega_M^f(1+z)^3 + (1 - \Omega_M^f)\right]^{1/2} \tag{11}
$$

The gravitational growth index γ is treated as a free parameter.

The time evolution of the normalization σ_8 is modelled as,

$$
\sigma_8(z) = \sigma_8(z_p)\frac{D(z)}{D(z_p)} \tag{12}
$$

where

$$
D(z) = \exp\left[-\int_0^z \mathrm{d}z \frac{f(z)}{1+z}\right] \tag{13}
$$

In this framework, the entire evolution history of $f\sigma_8$ is known given parameters $f(z_p)$, $\sigma_8(z_p)$, $\alpha_\parallel(z_p)$, $\alpha_\perp(z_p)$, and γ.

3.1.3 Parametrization of the bias parameters

The redshift evolution of the linear bias b_1 for the DR14Q sample has been found to be well approximated by a quadratic function (Laurent et al. 2017) developed in Croom et al. (2005). In this work, we adopt the fitting formula developed in Croom et al. (2005) with one parameter $b_1(z_p)$ to be determined, i.e.,

$$
b_1(z) = b_1(z_p) + 0.29\left[(1+z)^2 - (1+z_p)^2\right] \tag{14}
$$

The time evolution of the non-local bias b_2 has not been well studied in the literature. As it is expected to be much less important compared to the linear bias on scales of interest for BAO and RSD, we assume it to be a constant for simplicity, i.e.,

$$
b_2(z) = b_2(z_p). \tag{15}
$$

3.1.4 Parametrization of the FoG parameter

The RSD signal is affected by the so-called Finger-of-God (FoG) radial smearing owing to virialized peculiar velocities. We assume that the corresponding velocity dispersion, σ_v, is proportional to $(1+z)/H(z)$ during evolution (Seo & Eisenstein 2007), thus,

$$
\sigma_v(z) = \frac{H_f(z_p)}{H_f(z)}\frac{\alpha_\parallel(z)}{\alpha_\parallel(z_p)}\frac{1+z}{1+z_p}\sigma_v(z_p) \tag{16}
$$

3.1.5 Summary of the parameters

The free parameters used with the assumed form of redshift evolution are summarized in Table 1. In addition to the eight parameters shown in the bottom part of the table, we allocate another parameter N_{shot} to account for the stochasticity of the shot noise of the monopole, i.e., $P_0(k) \rightarrow P_0(k) + N_{shot}$ (see Sections 3.3 and 3.4 for the definition of P_0).

Table 1. The functional form of the redshift evolution of BAO, RSD, and bias parameters used in this work, and their priors. A weak Gaussian prior, which corresponds to the 3σ constraint derived from Planck 2015 observations (Planck Collaboration et al. 2016), is applied on $\sigma_8(z_p)$.

Quantities	Redshift evolution
BAO	$\alpha_\perp(z) = \alpha_\perp(z_p) + [\alpha_\parallel(z_p) - \alpha_\perp(z_p)]x$
BAO	$\alpha_\parallel(z) = \alpha_\parallel(z_p) + 2[\alpha_\parallel(z_p) - \alpha_\perp(z_p)]x$
RSD	$f(z) = f(z_p)\left(\frac{1+z}{1+z_p}\right)^{3\gamma}\left[\frac{\alpha_\parallel(z)}{\alpha_\parallel(z_p)}\frac{H_f(z_p)}{H_f(z)}\right]^{2\gamma}$
RSD	$\sigma_8(z) = \sigma_8(z_p)\frac{D(z)}{D(z_p)}$
RSD	$\sigma_v(z) = \frac{H_f(z_p)}{H_f(z)}\frac{\alpha_\parallel(z)}{\alpha_\parallel(z_p)}\frac{1+z}{1+z_p}\sigma_v(z_p)$
Bias	$b_1(z) = b_1(z_p) + 0.29[(1+z)^2 - (1+z_p)^2]$
Bias	$b_2(z) = b_2(z_p)$
Parameter	Prior
$\alpha_\perp(z_p)$	[0.7, 1.3]
$\alpha_\parallel(z_p)$	[0.7, 1.3]
$f(z_p)\sigma_8(z_p)$	[0, 2]
γ	[0, 2]
$b_1(z_p)\sigma_8(z_p)$	[0, 3]
$b_2(z_p)\sigma_8(z_p)$	$[-2, 2]$
$\sigma_8(z_p)$	$\mathcal{N}(0.367, 0.02^2)$
$\sigma_v(z_p)$	[0, 20]
N_{shot}	$[-60000, 60000]$

3.2 The Karhunen–Loève compression

To analyse the observational data of galaxy surveys, it is impractical to subdivide the galaxies into a large number of redshift slices and perform the measurement in each slice, therefore we seek a way to compress the data sample in redshift with minimum loss of information.

Data compression by applying optimal redshift weights was recently developed for the BAO measurement (Zhu et al. 2015, 2016), based on the Karhunen–Loève (K-L) compression method (Tegmark et al. 1997; Heavens, Jimenez & Lahav 2000). Here, we extend the analysis for a joint measurement of BAO and RSD for redshift surveys.

To be as general as possible, let us assume that we use N_p parameters to parametrize the galaxy power spectra multipoles in redshift space, which can be in principle measured at N_z redshifts and at N_k wavenumbers. We define the power spectrum vector $\boldsymbol{P}$ as,

$$\boldsymbol{P}_{\ell,z}(z_i) \equiv \left[P_\ell(k_1, z_i), P_\ell(k_2, z_i), \ldots, P_\ell(k_{N_k}, z_i)\right]^T \tag{17}$$

$$\boldsymbol{P}_z(z_i) \equiv \left[\boldsymbol{P}_{0,z}(z_i), \boldsymbol{P}_{2,z}(z_i), \ldots, \boldsymbol{P}_{2N_\ell,z}(z_i)\right]^T \tag{18}$$

$$\boldsymbol{P} \equiv \left[\boldsymbol{P}_z(z_1), \boldsymbol{P}_z(z_2), \ldots, \boldsymbol{P}_z(z_{N_z})\right]^T \tag{19}$$

The Fisher information matrix $\mathbf{F}$ using observables $\boldsymbol{P}$ is then,

$$\mathbf{F} = \mathbf{D}^T\mathbf{C}^{-1}\mathbf{D} \tag{20}$$

where $\mathbf{C}$ is the data covariance matrix, and the derivative matrix $\mathbf{D}$ is,

$$\mathbf{D} \equiv \left(\frac{\partial \boldsymbol{P}}{\partial p_1}, \frac{\partial \boldsymbol{P}}{\partial p_2}, \ldots, \frac{\partial \boldsymbol{P}}{\partial p_{N_p}}\right) \tag{21}$$

We are seeking an optimal redshift-weighting matrix $\boldsymbol{W}$ so that the z-weighted power spectra contain the same information for all the parameters.

The weighted power spectrum vector ($N_p N_k N_\ell N_z \times 1$) is

$$\boldsymbol{P}_w = \boldsymbol{W}^T \boldsymbol{P} \tag{22}$$

where $\mathbf{ssW}$ is a $N_z N_\ell N_k \times N_p$ weighting matrix, namely,

$$\boldsymbol{W} = \begin{pmatrix} W_{0,p_1}(k_1, z_1) & \ldots & W_{0,p_{N_p}}(k_1, z_1) \\ \ldots & & \ldots \\ W_{N_\ell, p_1}(k_{N_k}, z_{N_z}) & \ldots & W_{N_\ell, p_{N_p}}(k_{N_k}, z_{N_z}) \end{pmatrix} \tag{23}$$

The data covariance matrix $\mathbf{C}_w$ for the weighted observables $\boldsymbol{P}_w$ is a $N_p \times N_p$ matrix, namely,

$$\mathbf{C}_w = \mathbf{W}^T \mathbf{C} \mathbf{W} \tag{24}$$

The Fisher matrix is then,

$$\mathbf{F}_w = \mathbf{D}_w^T \mathbf{C}_w^{-1} \mathbf{D}_w \tag{25}$$

where

$$\mathbf{D}_w = \left(\frac{\partial \boldsymbol{P}_w}{\partial p_1}, \frac{\partial \boldsymbol{P}_w}{\partial p_2}, \ldots, \frac{\partial \boldsymbol{P}_w}{\partial p_{N_p}}\right) = \mathbf{W}^T \mathbf{D} \tag{26}$$

The compression is lossless, i.e., $\mathbf{F}_w = \mathbf{F}$, which means that the information content of a sufficiently redshift-sliced galaxy sample can be made exactly the same as that included in a set of redshift-weighted samples if the redshift weight $\boldsymbol{W}$ is,

$$\boldsymbol{W} = \boldsymbol{C}^{-1}\boldsymbol{D}. \tag{27}$$

In this case, it can be proved that,

$$\boldsymbol{D}_w^T = \boldsymbol{C}_w = \boldsymbol{D}_w = \boldsymbol{F}_w = \boldsymbol{D}^T\boldsymbol{C}^{-1}\boldsymbol{D} = \boldsymbol{F}. \tag{28}$$

This is easy to understand qualitatively: to avoid information loss in redshift when measuring N_p parameters at the same time, we have to perform the redshift weighting N_p times using the optimal weight for individual parameters respectively, and use these N_p observables coherently in the likelihood analysis by including the covariance among these observables properly. Note that $N_p = 1$, i.e., there is only one parameter to be determined, is a special case where P_w, D_w, C_w, and F_w become scalars, which is the case studied in Zhu et al. (2015, 2016) and Ruggeri et al. (2017).

3.3 The template of power spectrum at a specific redshift

We use the extended TNS model (Taruya, Nishimichi & Saito 2010) used in Beutler et al. (2014, 2017) and Alam et al. (2017) as a template of the two-dimensional power spectrum at a given redshift z,

$$\begin{aligned} P_g(k, \mu, z) = D_{FoG}(k, \mu, z) &\left[P_{g,\delta\delta}(k, z)\right. \\ &+ 2f(z)\mu^2 P_{g,\delta\theta}(k, z) + f^2(z)\mu^4 P_{\theta\theta}(k, z) \\ &\left.+ A(k, \mu, z) + B(k, \mu, z)\right], \end{aligned} \tag{29}$$

where

$$\begin{aligned} P_{g,\delta\delta}(k, z) = &\, b_1^2(z)P_{\delta\delta}(k, z) + 2b_1(z)b_2(z)P_{b2,\delta}(k, z) \\ &- \frac{8}{7}b_1(z)(b_1(z) - 1)P_{bs2,\delta}(k, z) \\ &+ \frac{64}{315}b_1(z)(b_1(z) - 1)\sigma_3^2(k, z)P_m^L(k, z) \\ &+ b_2^2(z)P_{b22}(k, z) - \frac{8}{7}[b_1(z) - 1]b_2(z)P_{b2s2}(k, z) \\ &+ \frac{16}{49}[b_1(z) - 1]^2 P_{bs22}(k, z), \end{aligned} \tag{30}$$

$$P_{g,\delta\theta}(k, z) = b_1(z)P_{\delta\theta}(k, z) + b_2(z)P_{b2,\theta}(k, z)$$
$$- \frac{4}{7}[b_1(z) - 1]P_{bs2,\theta}(k, z)$$
$$+ \frac{32}{315}[b_1(z) - 1]\sigma_3^2(k, z)P_m^L(k, z), \tag{31}$$

$$P_{g,\theta\theta}(k, z) = P_{\theta\theta}(k, z), \tag{32}$$

$$D_{FoG}(k, \mu, z) = \left\{1 + [k\mu\sigma_v(z)]^2 / 2\right\}^{-2}, \tag{33}$$

$$A(k, \mu, z) = b_1^3(z) \sum_{m,n=1}^{3} \mu^{2m}[f(z)/b_1(z)]^n A_{mn}(k, z),$$
$$B(k, \mu, z) = b_1^4(z) \sum_{m=1}^{4} \sum_{a,b=1}^{2} \mu^{2m}[-f(z)/b_1(z)]^{a+b} B_{ab}^m(k, z). \tag{34}$$

Note that subscripts δ and θ denote the overdensity and velocity divergence fields respectively, and $P_{\delta\delta}$, $P_{\delta\theta}$, and $P_{\theta\theta}$ are the corresponding nonlinear auto- or cross-power spectrum, which are evaluated using the regularized perturbation theory (REGPT) up to second order (Taruya et al. 2012). The linear matter power spectrum P_m^L is calculated using CAMB (Lewis, Challinor & Lasenby 2000). The terms b_1 and b_2 stand for the linear and the second-order local biases, respectively. We have eliminated the second-order non-local bias b_{s2} and the third-order non-local bias b_{3nl} using the following relation (Chan, Scoccimarro & Sheth 2012; Baldauf et al. 2012; Saito et al. 2014),

$$b_{s2} = -\frac{4}{7}(b_1 - 1),$$
$$b_{3nl} = \frac{32}{315}(b_1 - 1). \tag{35}$$

The *A* and *B* correction terms are computed using standard perturbation theory following equations (A3) and (A4) in Taruya et al. (2010).

3.4 The Alcock–Paczynski effect

The Alcock–Paczynski (AP) effect quantifies the difference in the dilation of scales along and cross the line of sight due to the wrong cosmology used to convert redshifts to distances (Alcock & Paczynski 1979), therefore this effect can be used to infer the true cosmology by contrasting the clustering along different lines of sight. Mathematically, the AP effect can be formulated as follows,
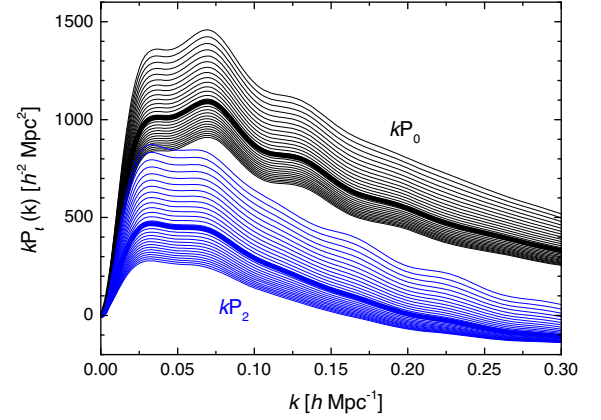
$$P_\ell(k, z) = \frac{2\ell + 1}{2\alpha_\perp^2 \alpha_\parallel} \int_{-1}^{+1} d\mu \, P_g(k', \mu', z)\mathcal{L}_\ell(\mu) \tag{36}$$

where $P_g(k', \mu', z)$ is given by equation (29), $\mathcal{L}_\ell$ is the Legendre polynomial of order ℓ, and,

$$k' = \frac{k(1 + \epsilon)}{\alpha} \left\{1 + \mu^2\left[(1 + \epsilon)^{-6} - 1\right]\right\}^{1/2}$$
$$\mu' = \frac{\mu}{(1 + \epsilon)^3} \left\{1 + \mu^2\left[(1 + \epsilon)^{-6} - 1\right]\right\}^{-1/2}$$
$$\alpha = \alpha_\perp^{2/3}\alpha_\parallel^{1/3}; \quad 1 + \epsilon = F_{AP}^{1/3}; \quad F_{AP} = \frac{\alpha_\parallel}{\alpha_\perp} \tag{37}$$

Figure 2. The power spectrum monopole (upper group of curves) and quadrupole (lower group) of the fiducial model at various redshifts. In each group, curves from top to bottom show the fiducial models at redshifts $z = 0.825$–2.175, with redshift increment of $\Delta z = 0.05$. The thick curves within each group show the power spectra of the fiducial model at an effective redshift of $z_{eff} = 1.52$ of the DR14Q sample covering the redshift range of $0.8 < z < 2.2$.

The power spectrum monopole and quadrupole of the fiducial model at various redshifts from 0.8 to 2.2 are shown in Fig. 2.

3.5 The data covariance C

We model the time evolution of the data covariance matrix **C** using an analytic method (Taruya et al. 2010),

$$\text{Cov}_{\ell\ell'}(k, z) = \frac{4\pi^2}{k^2 \Delta k \Delta V(z)} \frac{(2\ell + 1)(2\ell' + 1)}{2}$$
$$\times \int_{-1}^{+1} d\mu \mathcal{L}_\ell(\mu)\mathcal{L}_{\ell'}(\mu) \left[P_g(k, \mu, z) + \frac{1}{\bar{n}_g(z)}\right]^2 \tag{38}$$

In Fig. 3, we show a comparison of $\text{Cov}_{00}(k, z)$, the diagonal elements of the data covariance matrix (the monopole–monopole block), derived from the EZ mocks (the four data points with error bars), with that computed using the analytical formula shown in equation (38, the filled band). This shows that our analytic formula can well capture the redshift evolution of Cov_{00}, especially at $k \simeq 0.1\,h\,\text{Mpc}^{-1}$. We have numerically confirmed that this also holds for Cov_{22} and Cov_{02}.[3]

We notice that equation (38) assumes the diagonality of the covariance among different k modes, which well approximates the covariance matrices derived from the mocks, although it can be further improved using more sophisticated methods to include the non-Gaussian contribution (see Howlett & Percival 2017; O'Connell & Eisenstein 2018 for recent developments and references therein).

Note that the amplitude of the estimated Cov is irrelevant, as long as the normalization is kept the same for all redshifts. This is because the normalization of the weights to be derived from Cov can be arbitrary.

---

[3] We have checked and confirmed that the redshift evolution of $\text{Cov}_{\ell\ell'}$ where $\ell, \ell' = 0, 2$ shows a similarity to a large extent for different k modes for $k \in [0.05, 0.15]\,h\,\text{Mpc}^{-1}$.
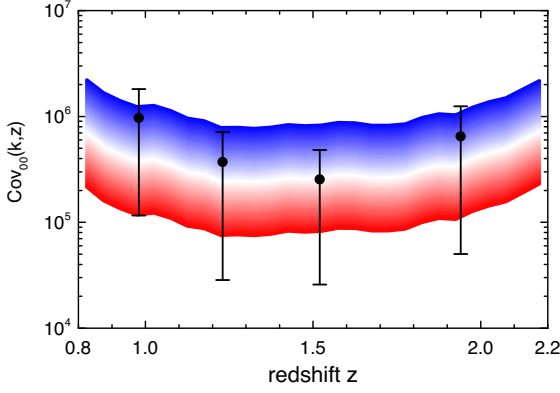
Figure 3. A comparison of $Cov_{00}(k, z)$, which are the diagonal elements of the covariance matrix (the monopole–monopole block), derived from the EZ mocks (data points with error bars), with that computed using the analytical formula shown in equation (38, the filled band). Both the band and the error bars show $Cov_{00}(k, z)$ for k modes in the range of $k \in [0.05, 0.15]\,h\,\mathrm{Mpc}^{-1}$. For the analytic covariance shown in the band, k is sampled logarithmically from 0.05 to 0.15 $h\,\mathrm{Mpc}^{-1}$ from top to bottom, and the white curve in the middle corresponds to $k = 0.1\,h\,\mathrm{Mpc}^{-1}$. For the covariance derived from mocks at four effective redshifts, the k bins are made uniform linearly in the same range, and the central value and the error bars denote values for $k = 0.1\,h\,\mathrm{Mpc}^{-1}$, and the standard deviation, respectively.

3.6 The optimal redshift weights

Now we attempt to derive the optimal redshift weights for each parameters shown in Table 1. Specifically, we evaluate the derivative matrix **D** shown in equation (21) numerically, and compute the data covariance matrix **C** using equation (38). We have numerically verified that the k-dependence of all the weights is very weak in the k range of $0.05 \lesssim k \lesssim 0.25 h\,\mathrm{Mpc}^{-1}$ where data are most informative, thus we compute the redshift weights at $k = 0.1 h\,\mathrm{Mpc}^{-1}$ without loss of generality.

The optimal redshift weights for the relevant parameters using the monopole and quadrupole of the galaxy power spectrum are calculated using equation (27), and are shown in Fig. 4 . As illustrated, the shapes of these weights show a high level of similarity, which means that there would be significant redundancy in weighted power spectra, if these weights were applied. This will not only cause unnecessary computations, but also yield a largely singular data covariance matrix, which is difficult to invert accurately for likelihood analysis.

To remove the redundancy in the redshift weights, we perform a singular-value decomposition (SVD) of the original redshift weights for all the parameters shown in Fig. 4, i.e.,

$$\mathbf{X} = \mathbf{U}\Lambda V^T \tag{39}$$

where **X** is the data matrix of the weights, and **Λ** is a diagonal matrix storing the variances. The new orthogonal weights can be found by projecting the original ones on to the new basis **V**, whose variances are ordered in **Λ**. Keeping a first few principal components can largely reduce the redundancy with negligible information loss .[4]

This procedure yields two orthogonal weights for monopole and quadrupole each, which represents over 90 per cent of the variance in the data, as shown in the left-hand panels of Fig. 5. Note that these new redshift weights are not generically positive definite, making

[4]We provide a MATLAB code in the Appendix for the SVD analysis.
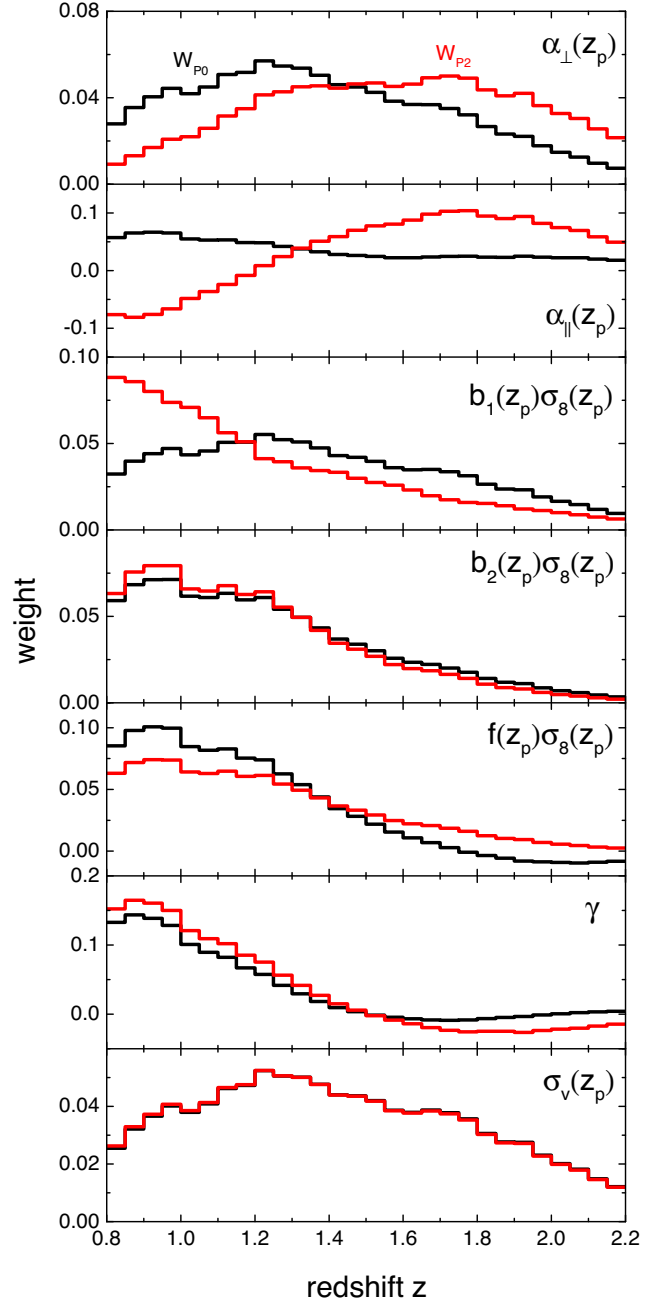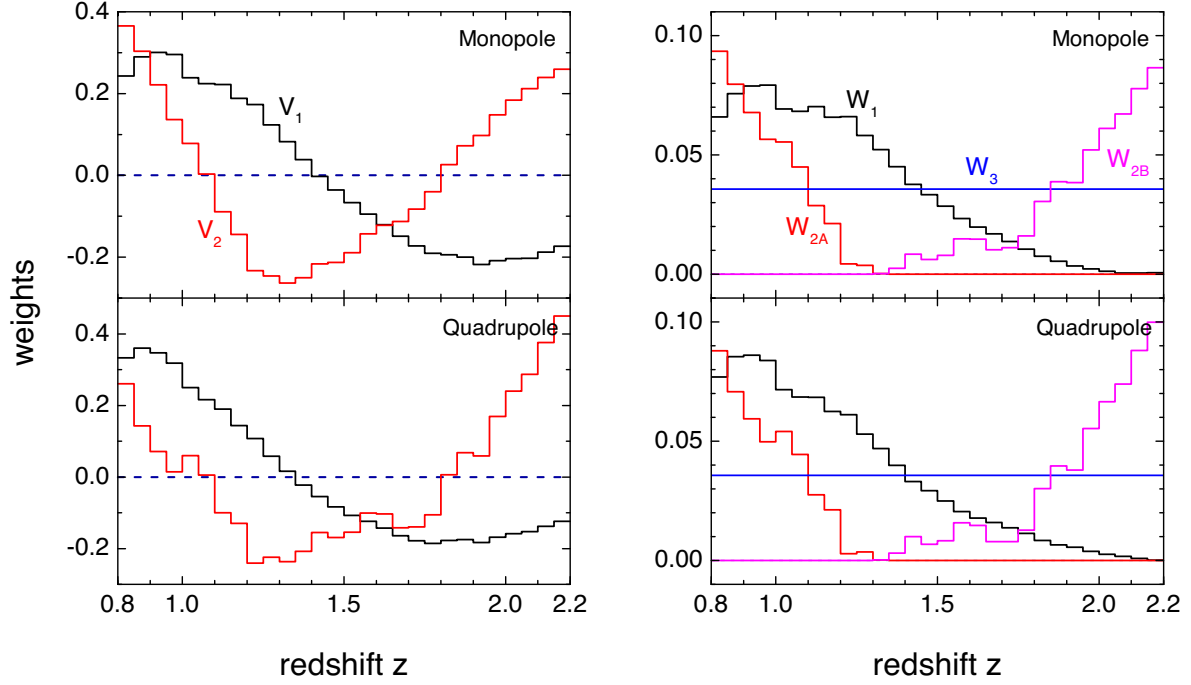
Figure 4. The optimal redshift weights for the monopole (black) and quadrupole (red) each free parameters as shown in the figure legend. For illustration, the weights are normalized so that the sum of each weight in the entire redshift range ($0.8 < z < 2.2$) is unity, although the normalization can be arbitrary.

it difficult to apply to the galaxy catalogues .[5] In some occasions, all the weights can be made positive by a linear transformation without loss of information. However, as this is not always feasible, we add a third weight, which is a constant in z, to guarantee that the weights can be always turned positive by a linear transforma-

[5]This is because these weights are supposed to be applied to power spectra, not to individual galaxies. The weights for galaxies are square root of the redshift weights, thus they must be positive definite.

Figure 5. Left: the first two principal redshift weights, denoted as V_1 and V_2, for the monopole (upper panel) and quadrupole (lower) respectively derived from an SVD analysis. Right: the positive-definite redshift weights, W_1, $W_{2A(B)}$, W_3, derived from linear combinations of V_1, V_2, and a constant. The W weights are normalized in the same way as in Fig. 4.

tion. As the added constant weight spoils the orthogonality of the weights, we tune the constant to minimize the correlation between the weights, which removes the redundancy as much as possible. We include a detailed procedure of obtaining the weights in Appendix B. The resultant weights are shown in the right-hand panel of Fig. 5.

Care must be taken when analysing these redshift-weighted samples using a template at a single effective redshift, as in the traditional method. As the redshift weights can be generally arbitrary in shape, it can make the redshift distribution of the weighted sample multimodal, making it inaccurate to be modelled using a template at a single effective redshift. To be explicit, we revisit the calculation of the effective redshift. Observationally, the measured power spectra are actually a redshift-weighted average across the redshift range of the catalogue, i.e.,

$$P = \frac{\sum P(z_i) w_i^2}{\sum w_i^2} \tag{40}$$

Expanding the power spectra at an arbitrary redshift z around an effective redshift z_{eff} yields,

$$P(z) = P(z_{eff}) + P'(z - z_{eff}) + \frac{1}{2} P''(z - z_{eff})^2 + \mathcal{O}(P''') \tag{41}$$

Combining equations (40) and (41), we have,

$$P = P(z_{eff}) + P'\Delta_1 + \frac{1}{2} P''\Delta_2 + \mathcal{O}(P''') \tag{42}$$

where,

$$\Delta_1 = \left(\frac{\sum z_i w_i^2}{\sum w_i^2} - z_{eff} \right)$$

$$\Delta_2 = \left(\frac{\sum z_i^2 w_i^2}{\sum w_i^2} - 2z_{eff} \frac{\sum z_i w_i^2}{\sum w_i^2} + z_{eff}^2 \right) \tag{43}$$

The first-order term Δ_1 vanishes if $z_{eff} = \frac{\sum z_i w_i^2}{\sum w_i^2}$, but this does not necessarily diminish Δ_2 and higher order terms. Actually, when $\Delta_1 = 0$,

$$\Delta_2 = \left[\frac{\sum z_i^2 w_i^2}{\sum w_i^2} - \left(\frac{\sum z_i w_i^2}{\sum w_i^2} \right)^2 \right] \tag{44}$$

The catalogue can only be analysed using a template at the effective redshift if $\Delta_2 \ll 1$, which is not always the case generally. We have numerically checked that $\Delta_2(W_1)$ and $\Delta_2(W_3)$ are sufficiently small to be ignored. However, this term for W_2 ($W_{2A} + W_{2B}$ in the right-hand panel of Fig. 5) is non-negligible due to its double-peaked feature. Therefore, we split this weight into two pieces W_{2A} and W_{2B} so that each one can be well modelled by its own effective redshift. The explicit values for Δ_2 for these four weighted samples are listed in the bottom of Table 2.

4 RESULTS

In this section, we perform tests on the mocks before the joint measurement on BAO and RSD parameters using the eBOSS DR14Q sample at four effective redshifts. We also present a measurement of linear bias.

4.1 Joint BAO and RSD measurements

We first apply the square root of redshift weights W_1, W_{2A}, W_{2B}, and W_3 shown in Fig. 5 to both the EZ mocks and the DR14Q sample, and measure the corresponding power spectra monopole and quadrupole using the Fast Fourier Transform (FFT) method presented in Bianchi et al. (2015), as shown in Fig. 6. As the power spectra derived from the z-weighted samples are essentially linear combinations of power spectra at multiple redshifts, we compute

Table 2. The measurement of BAO, RSD, and other relevant parameters from the DR14 QSO sample at four effective redshifts. The unit of D_M and D_V is Mpc, and that of H is km s^{-1} Mpc^{-1}.

	DR14 QSO sample			
	$z_{eff} = 0.978$	$z_{eff} = 1.230$	$z_{eff} = 1.526$	$z_{eff} = 1.944$
$\alpha_\perp$	0.939 ± 0.169	1.003 ± 0.091	0.986 ± 0.054	1.017 ± 0.082
$\alpha_\parallel$	1.061 ± 0.130	1.053 ± 0.100	1.095 ± 0.094	1.155 ± 0.093
α	0.971 ± 0.108	1.017 ± 0.056	1.020 ± 0.037	1.059 ± 0.056
ε	0.048 ± 0.087	0.018 ± 0.054	0.036 ± 0.041	0.044 ± 0.044
$D_A \times (r_d^{fid}/r_d)$	1586.18 ± 284.93	1769.08 ± 159.67	1768.77 ± 96.59	1807.98 ± 146.46
$H \times (r_d/r_d^{fid})$	113.72 ± 14.63	131.44 ± 12.42	148.11 ± 12.75	172.63 ± 14.79
$D_V \times (r_d^{fid}/r_d)$	2933.59 ± 327.71	3522.04 ± 192.74	3954.31 ± 141.71	4575.17 ± 241.61
F_{AP}	1.200 ± 0.310	1.736 ± 0.272	2.212 ± 0.265	3.071 ± 0.416
$f\sigma_8$	0.379 ± 0.176	0.385 ± 0.099	0.342 ± 0.070	0.364 ± 0.106
$b_1\sigma_8$	0.826 ± 0.080	0.894 ± 0.051	0.953 ± 0.044	1.080 ± 0.057
$b_2\sigma_8$	0.460 ± 0.684	0.605 ± 0.533	0.704 ± 0.507	0.929 ± 0.681
σ_v	3.784 ± 1.087	4.732 ± 0.761	5.822 ± 0.796	7.591 ± 1.127
χ^2/dof	$56/(58 - 8)$	$53/(58 - 8)$	$44/(58 - 8)$	$40/(58 - 8)$
Δ_2	0.001	0.007	0.141	0.004
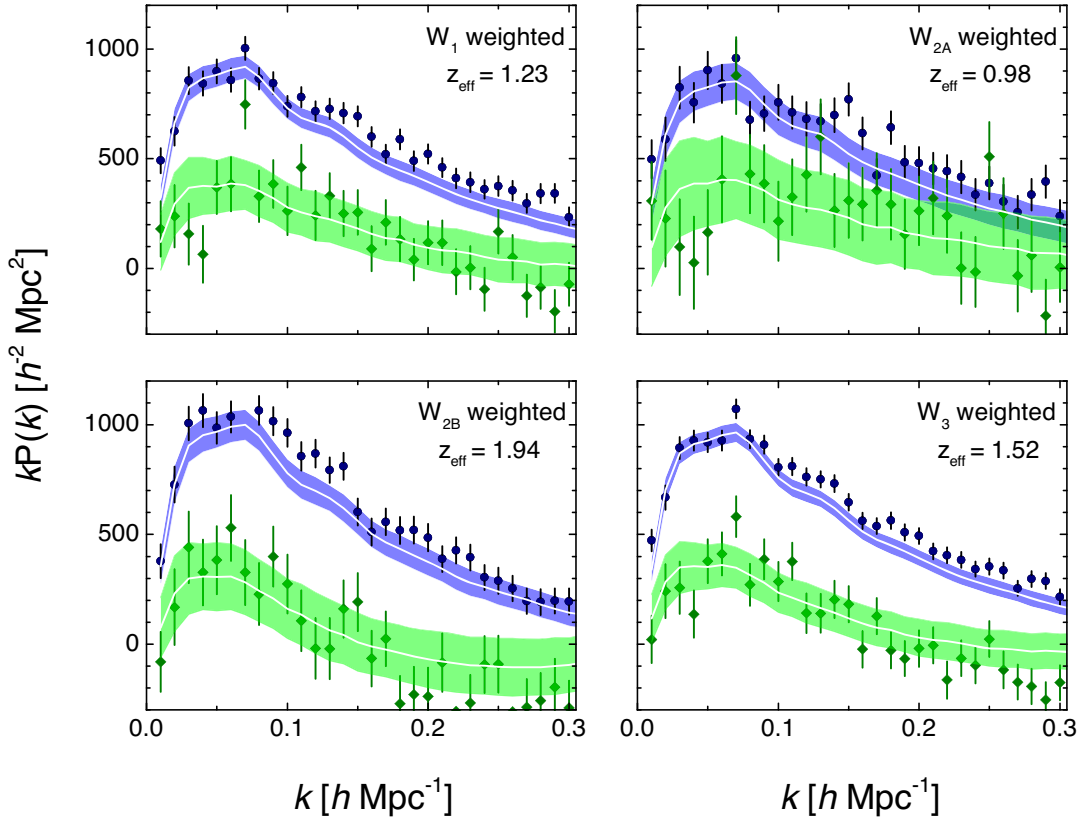
Figure 6. The measured galaxy power spectra monopole (upper band or data points) and quadrupole (lower) from the EZ mocks (filled bands) and DR14Q catalogues (data points with error bars) with redshift weights by W_1, W_{2A}, W_{2B}, and W_3 respectively. All spectra are multiplied by the wavenumber k for illustration.

the effective redshifts for each of the weighted sample using equation (5), and find,

$$z_{eff}(W_1) = 1.23,$$
$$z_{eff}(W_{2A}) = 0.98,$$
$$z_{eff}(W_{2B}) = 1.94,$$
$$z_{eff}(W_3) = 1.52. \tag{45}$$

Using a modified version of COSMOMC (Lewis & Bridle 2002), we then fit for parameters shown in Section 3.1.5 at each effective redshift to the power spectra using the template detailed in Section 3.3. The theoretical power spectra multipoles are convolved with the survey window functions, which are shown in Appendix D, measured using the method developed in Wilson et al. (2017). The joint measurement of $\alpha_\perp$, $\alpha_\parallel$, and $f\sigma_8$ is shown in Fig. 7.

Each of the cyan dots represents the best-fitting model derived from one specific EZ mock, and the black contours show the
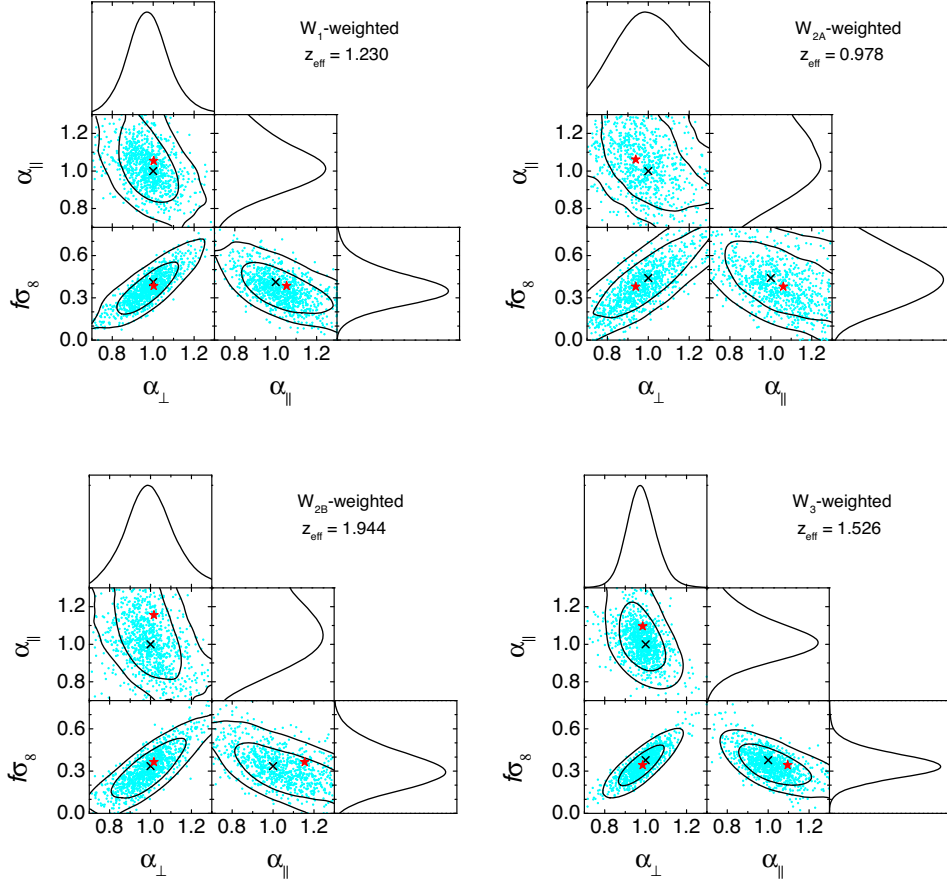
Figure 7. The result of mock tests and actual measurement of BAO and RSD parameters from the DR14Q sample. Results for four redshift-weighted samples are shown in four panels, as illustrated in the legend. In each panel, the best-fitting values of parameters for each of the 1000 EZ mocks are shown in cyan dots, and the black crosses and the red stars mark the expected values of EZ mocks, and the actual measurement from the DR14Q sample, respectively. The 68 per cent and 95 per cent CL contours and one-dimensional posterior distribution of parameters are shown in black curves.

68 per cent and 95 per cent CL constraint using the mean of the 1000 EZ mocks. As shown, the measurement of BAO and RSD parameters (with other parameters marginalized over) at four effective redshifts are all largely consistent with the expected values denoted by black crosses with the maximal deviation less than 0.3σ, which validates our pipeline.

We then apply our pipeline to the DR14Q catalogue, and show the measurement in Table 2 and in Figs 7–8.

In Fig. 7, we see that the best-fitting model to the DR14Q sample (red stars) is within the 68 per cent CL contours of the EZ mocks at all effective redshifts, which means that the fiducial cosmology used to produce the EZ mocks can reasonably approximate the true cosmology probed by the quasar sample within 68 per cent CL.

Fig. 9 shows our BAO and RSD measurements in comparison with other published ones from galaxy surveys, as well as with the *Planck* constraint in a ΛCDM model derived in Zhao et al. (2017a). Our measurements of $D_M \equiv (1 + z)D_A$ and $f\sigma_8$ are in excellent agreement with the *Planck* constraint at all redshifts, but our measurement on $D_H(z) \equiv c/H(z)$ shows a deviation at $z = 1.526$ and 1.944 at $\gtrsim 1\sigma$ significance. Interestingly, Gil-Marín et al. (2018) find a similar deviation at $z = 1.50$ using the same data sample. Moreover, the D_H measurement at $z = 2.4$ using Lyman-α forest shows a deviation in the same direction. We will reinvestigate this issue when the eBOSS quasar survey is completed.

As shown in the right-hand panel of Fig. 9, our $f\sigma_8$ measurement at $z = 1.52$ is largely consistent with that presented in companion papers of Gil-Marín et al. (2018) and Hou et al. (2018), which are studies on the same data sample using different methods. Interestingly, the compilation of $f\sigma_8$ measurements shown in the right-hand panel of Fig. 9 seems to favour lower values of $f\sigma_8$ than that in the ΛCDM model across a wide redshift range. Li & Zhao (2018) performed a constraint on modified gravity models using a combined observational data including the BAO and RSD measurements derived in this work, and it is found that a model in which the effective Newton's constant is parametrized as $G_{eff} = 1 + \mu_s a^s$ (where μ_s and s are free parameters, and $\mu_s = 0$ in ΛCDM) is able to fit the data better (see our overplot of their best-fitting model predictions with data points in the right-hand panel of Fig. 9).

We show contour plots between $f\sigma_8$, D_V, and $F_{AP} \equiv D_M H/c$ in Fig. 8, and as shown, our measurements are consistent with the *Planck* observations.

As the weights are not orthogonal to each other, the measurements at four effective redshifts are generally correlated. We quantify the correlation by fitting to each of the 1000 EZ mocks, and compute the correlation matrix using the fitted parameters. The correlation matrix is shown in Fig. 10, with the numeric values of the correlation matrix and the precision matrix shown in Table 3.[6] As expected,
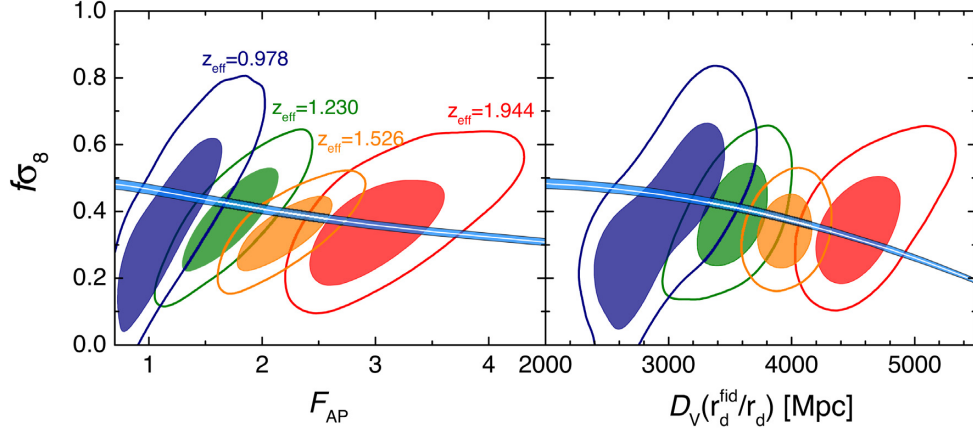
Figure 8. The 68 per cent and 95 per cent CL contour plots between $f\sigma_8$ and F_{AP} (left-hand panel), and between $f\sigma_8$ and D_V (right). In each panel, the contours from left to right are for measurements at four effective redshifts, as illustrated in the legend. As in the right-hand panel of Fig. 9, the filled bands show the mean, and 68 per cent CL constraint on $f\sigma_8$, derived from Planck 2015 observations, combined with external data sets in a ΛCDM Universe (Zhao et al. 2017a).
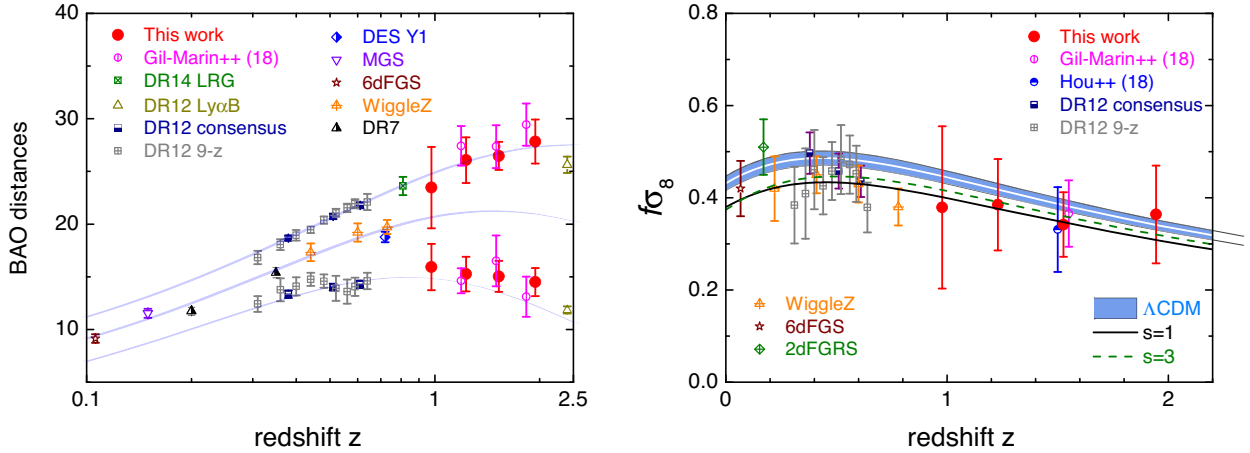
Figure 9. Left: the BAO distance measurements derived from this work presented in Tables 2 and 3 (large filled circles) in comparison with other recent BAO measurements (shown in the legend), including Gil-Marín et al. (2018), eBOSS DR14 LRG (Bautista et al. 2018), BOSS DR12 LyαF BAO (Gontcho et al. 2018), BOSS DR12 consensus (Alam et al. 2017), BOSS DR12 tomographic BAO measurements at nine effective redshifts (DR12 9-z; Zhao et al. 2017b), DES year 1 BAO (The Dark Energy Survey Collaboration et al. 2017), MGS (Ross et al. 2015), 6dFGS (Beutler et al. 2011), WiggleZ BAO (Kazin et al. 2014), and BOSS DR7 (Percival et al. 2010). The three filled bands from top to bottom show the 95 per cent CL constraints of $D_M(z)/\left(r_d\sqrt{z}\right)$, $D_V(z)/\left(r_d\sqrt{z}\right)$, and $zD_H(z)/\left(r_d\sqrt{z}\right)$, respectively. The band are derived from Planck 2015 observations, combined with external data sets including supernovae, galaxy clustering and weak gravitational lensing in a ΛCDM Universe (Zhao et al. 2017a). The top and bottom bands and data points are vertically displaced by 2 for illustration. Right: The RSD measurement parametrized by $f\sigma_8$ derived from this work (large filled circles) in comparison with other recent RSD measurements (shown in the legend), including Gil-Marín et al. (2018), Hou et al. (2018), BOSS DR12 consensus (Alam et al. 2017), BOSS DR12 tomographic RSD measurements at nine effective redshifts (DR12 9-z; Wang et al. 2018b), WiggleZ (Contreras et al. 2013), 6dFGS (Beutler et al. 2012), and 2dFGRS (Peacock et al. 2001). The filled band shows the mean, and 68 per cent CL constraint on $f\sigma_8$, derived from Planck 2015 observations, combined with external data sets in a ΛCDM Universe (Zhao et al. 2017a) (as in the left-hand panel), and the black solid and green dashed curves show the best-fitting modified gravity models denoted by two different values of s, which was derived in Li & Zhao (2018). See the texts for more details.
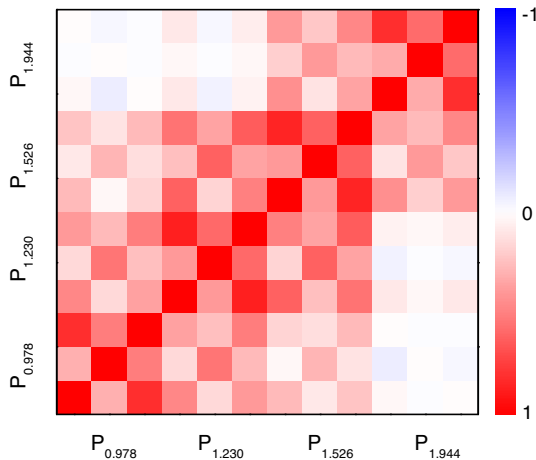
the same parameters at different effective redshifts are positively correlated except for those at $z = 0.978$ and 1.944, as the quasar distributions for these two weighted samples do not overlap.

Tables 2 and 3 present the main result of this work, which can be directly used to constrain cosmological models. To compare with measurements at $z_{\rm eff} = 1.52$ presented in companion papers, we linearly combine our measurements at four redshifts. We adjust

---

[6]The correlation and the precision matrices are the rescaled covariance and inverse covariance matrices, respectively, with all the diagonal elements being unity.

the coefficients for the combination so that the effective redshift calculated using equation (5) is exactly 1.52. Given that the set of coefficients to yield $z_{\rm eff} = 1.52$ is not unique, we choose a set of coefficients to maximize the figure of merit (FoM) of D_A, H, and $f\sigma_8$, with a constraint of $\Delta_2 \ll 1$ for the linearly combined sample. The procedure is explicitly shown in Appendix A.

We have numerically checked that as long as $\Delta_2 \ll 1$ and the FoM saturates to its maximal value, different choices of the coefficients have negligible impact on the resultant parameter constraints. With these constraints, the coefficients are found to be {0.02, 0.17, 0.57, 0.24} for the weighted samples with $z_{\rm eff} = 0.978$, 1.230, 1.526, and 1.944, respectively. Note that due to the correlation among the

Figure 10. The correlation matrix for parameters measured from observables weighted by redshift weights shown in the legend. For each 3×3 parameter block, the order of parameters is D_A, H, and $f\sigma_8$.

four catalogues, the trivial solution of $\{0, 0, 1, 0\}$ does not maximize the FoM (see Fig. A1 in the Appendix).

The final measurement at $z_{eff} = 1.52$ is shown in Table 4 and Fig. 11. To distinguish this measurement from the raw measurement at $z_{eff} = 1.52$, we denote this and the raw measurement as 'z-weighted' and 'unweighted' respectively. As shown, the 'z-weighted' constraint is slightly tighter, namely, the FoM of D_A, H, and $f\sigma_8$ is improved by 15 per cent. However, we strongly recommend users to use the tomographic measurement shown in Tables 2 and 3 for model constraints as those are more informative with light-cone information.

4.2 A measurement of the linear bias

As a by-product of our BAO and RSD measurements, we measure the linear bias b_1 at four effective redshifts, and present the result in Table 2 and Fig. 12. In Fig. 12, we overplot our measurement with published results using clustering quasars including Ross et al. (2009) and Laurent et al. (2017, 2016), as well as with the fitting formula developed in Croom et al. (2005). We find an excellent agreement between our measurement and the Croom et al. (2005) fitting formula.[7]

5 THE CONSENSUS RESULT

The joint BAO and RSD analyses presented in this work is based on a power spectrum analysis using monopole and quadrupole (in the k range of $0.02 \leq k \, [h\mathrm{Mpc}^{-1}] \leq 0.30$) derived from the eBOSS DR14 quasar sample covering the redshift range of $0.8 \leq z \leq 2.2$. The power spectrum template used in this work is primarily based on the RegPT up to second order. With the optimal redshift weights, we constrain D_A, H, and $f\sigma_8$ at four effective redshifts, namely, $z_{eff} = 0.978, 1.230, 1.562,$ and 1.944.

This work is released along with other complementary RSD analyses based on the exact same sample, including the same weighting schemes described in (Gil-Marín et al. 2018, except for the redshift weights used in this work). The fiducial cosmology in which the

[7]We also measured the bias evolution from the EZ mocks, and find an excellent agreement with the Croom et al. (2005) fitting formula as well.

sample has been analysed is also the same across papers. We briefly describe them below.

(i) The RSD analysis in Gil-Marín et al. (2018) is based on the eBOSS DR14 quasar sample in the redshift range $0.8 \leq z \leq 2.2$, using the power spectrum monopole, quadrupole, and hexadecapole measurements on the k range, $0.02 \leq k \, [h\mathrm{Mpc}^{-1}] \leq 0.30$, shifting the centres of k bins by fractions of $1/4$ of the bin size and averaging the four derived likelihoods. Applying the TNS model along with the two-loop resumed perturbation theory, we are able to effectively constrain the cosmological parameters $f\sigma_8(z)$, $H(z)r_s(z_d)$, and $D_A(z)/r_s(z_d)$ at the effective redshift $z_{eff} = 1.52$, along with the remaining 'nuisance' parameters, $b_1\sigma_8(z)$, $b_2\sigma_8(z)$, $A_{noise}(z)$, and $\sigma_P(z)$, in all cases with wide flat priors.

(ii) Hou et al. (2018) analyse the eBOSS DR14 quasar sample in the redshift range $0.8 \leq z \leq 2.2$ using Legendre polynomial with order $\ell = 0, 2, 4$, and clustering wedges. They use 'gRPT' to model the non-linear matter clustering. As for the RSD, they use a streaming model extended to one-loop contribution developed by Scoccimarro (2004) and Taruya et al. (2010) and a non-linear corrected FoG term. They adopt the bias modelling as described in Chan & Scoccimarro (2012), which includes both local and non-local contribution. Additionally, they also include the modelling for spectroscopic redshift error. Finally, they arrive at constraints on $f\sigma_8(z_{eff}) \, D_V(z)/r_d$ and $F_{AP}(z)$ at the effective redshift $z_{eff} = 1.52$.

(iii) The clustering analysis presented in Zarrouk et al. (2018) is based on the eBOSS DR14 quasar sample in the redshift range $0.8 \leq z \leq 2.2$, using Legendre multipoles with $\ell = 0, 2, 4$, and three wedges of the correlation function on the s range from $16 \, h^{-1}\mathrm{Mpc}$ to $138 \, h^{-1}\mathrm{Mpc}$. They use the Convolution Lagrangian Perturbation Theory with a Gaussian Streaming model and they demonstrate its applicability for dark matter haloes of masses of the order of $10^{12.5}\mathrm{M}_\odot$ hosting eBOSS quasar tracers at mean redshift $z \simeq 1.5$ using the OuterRim simulation. They find consistent results between the two methods and it yields to constraints on the cosmological parameters $f\sigma_8(z_{eff})$, $H(z_{eff})$, and $D_A(z_{eff})$ at the effective redshift $z_{eff} = 1.52$.

(iv) Ruggeri et al. (2018) measure the growth rate and its evolution using the anisotropic clustering of the extended eBOSS DR14 quasar sample. To optimize the measurements, we deploy a redshift-dependent weighting scheme, which avoids binning, and perform the data analysis consistently including the redshift evolution across the sample. They perform the analysis in Fourier space, and use the redshift evolving power spectrum multipoles to measure the RSD parameter $f\sigma_8$ alongside nuisance parameters, and parameters controlling the anisotropic projection of the cosmological perturbations. They make use of two different sets of weights, described in Ruggeri et al. (2017). This model ties together growth and geometry, but can also be used after fixing the expansion rate to match the prediction of the ΛCDM model. The second parametrizes the $f\sigma_8$ parameter combination measured by RSD, allowing for a more standard test of deviations from ΛCDM. They compare all results with the *standard* analysis performed at one single redshift of $z = 1.52$.

In Figs 13 and 14, we make a direct comparison to two of the companion works, which are RSD analysis in Fourier space. Results shown in Fig. 13 are without redshift weights, while results in Fig. 14 are those with redshift weights. As shown, the results are consistent with each other in both cases within the uncertainty.

In addition, two BAO papers using the same sample are released as companion papers: Wang et al. (2018a) and Zhu et al. (2018), which are complementary to the isotropic analysis recently pre-

Table 3. The upper triangular part of the table: the correlation matrix shown in Fig. 10; and the lower triangular part: the precision matrix. Both the correlation and precision matrices are multiplied by 10^4 for illustration. The $1/s_i$ column shows the square root of the reciprocal of the diagonal of the inverse covariance matrix. The dashed lines separate the entries for different effective redshifts for illustration.

Parameters	$10^4 f_{ij}$ (lower triangular) and $10^4 c_{ij}$ (upper)												$1/s_i$
$D_A(0.978)$	10000	3106	8142	4656	1535	3957	2662	920	2328	248	−194	12	115.6
$H(0.978)$	3399	10000	5066	1543	5341	2699	265	2934	1165	−786	23	−377	9.57
$f\sigma_8(0.978)$	−8711	−5542	10000	3740	2564	5118	1718	1313	2667	24	−192	−113	0.060
$D_A(1.230)$	−5983	−2613	6051	10000	3993	8621	6130	2421	5460	954	313	845	32.16
$H(1.230)$	−3509	−5157	4773	5721	10000	5994	1711	6056	3409	−566	−40	−300	5.09
$f\sigma_8(1.230)$	5657	3282	−6400	−9462	−7165	10000	4831	3584	6288	510	226	722	0.016
$D_A(1.526)$	2862	1198	−3048	−8204	−4824	8032	10000	3888	8574	4257	1941	3919	20.13
$H(1.526)$	1946	1226	−2276	−5180	−7167	6212	6111	10000	6015	1150	3897	2156	5.21
$f\sigma_8(1.526)$	−3002	−1304	3253	7898	5798	−8422	−9419	−7516	10000	3519	2623	4721	0.011
$D_A(1.944)$	−1454	−18	1360	5098	3331	−5176	−6910	−4718	6758	10000	3306	8127	58.0
$H(1.944)$	−1041	−690	1255	3434	4368	−4012	−4382	−6340	5166	4855	10000	5687	8.99
$f\sigma_8(1.944)$	1790	363	−1758	−5487	−4130	5933	7069	5987	−7707	−8799	−6752	10000	0.032

Table 4. The measurement of BAO and RSD parameters at the effective redshift 1.526 with the redshift weights. The notations are the same as those in Table 3.

Parameters	Mean	Uncertainty	$10^4 f_{ij}$ (lower triangular) and $10^4 c_{ij}$ (upper)			$1/s_i$
$D_A(1.526)$	1774.59	9483	10000	3619	8356	50.33
$H(1.526)$	150.32	1050	2572	10000	5718	8.32
$f\sigma_8(1.526)$	0.356	0067	−8220	−5261	10000	0.031
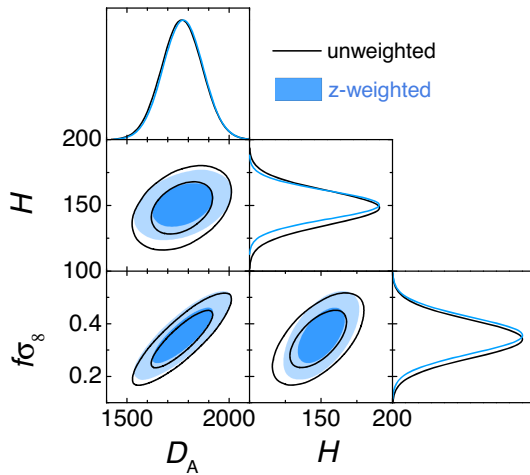
Figure 11. A comparison of the constraint on D_A, H, and $f\sigma_8$ with (blue, filled) and without (black, unfilled) the redshift weights. The inner and outer contours show the 68 per cent and 95 per cent CL two-dimensional marginalized constraints, and the one-dimensional curves show the posterior likelihood distribution for the corresponding parameters.

sented by Ata et al. (2018). These works measure the isotropic and anisotropic BAO in the Fourier and configuration spaces, respectively, with the optimal redshift weights, and their results are consistent and complementary to each other.

6 A COSMOLOGICAL IMPLICATION

This subsection is devoted to a cosmological implication of our joint BAO and RSD measurements at four effective redshifts presented in Tables 2 and 3.

We first apply our BAO measurement to calibrate the geometry of the Universe, parametrized by Ω_M, Ω_Λ, and $H_0 r_d$, using three
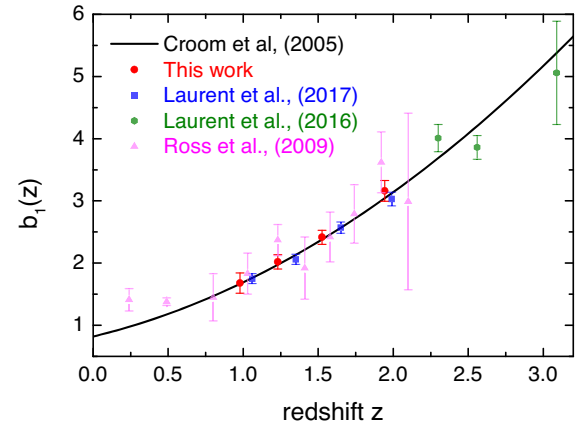

Figure 12. The measurement of the linear bias b_1 from this work (red circles), in comparison with other recent measurements denoted in the legend, including Laurent et al. (2017, 2016) and Ross et al. (2009). The black solid curve shows the model prediction of Croom et al. (2005).

different BAO data combinations, and present the result in Fig. 15 and Table 5.

As shown, our DR14Q BAO measurement combined with DR12 galaxies (BOSS gal. + this work) suggests that dark energy exists at a significance level of 3.67σ, compared to 2.95σ using BOSS galaxies alone. The FoM, which is defined as the square root of the inverse covariance matrix of the $\{\Omega_M, \Omega_\Lambda\}$ block, is improved by a factor of 3.5 by our tomographic DR14Q measurement. Compared to the quasar BAO measurement at a single effective redshift of 1.52 presented in Ata et al. (2018), our measurement is more informative to constrain the geometry of the Universe, namely, the Ata et al. (2018) measurement improves the BOSS DR12 FoM by a factor of 2.

We also note that the preferred values of both Ω_M and Ω_Λ derived from this data combination are lower than that favoured by
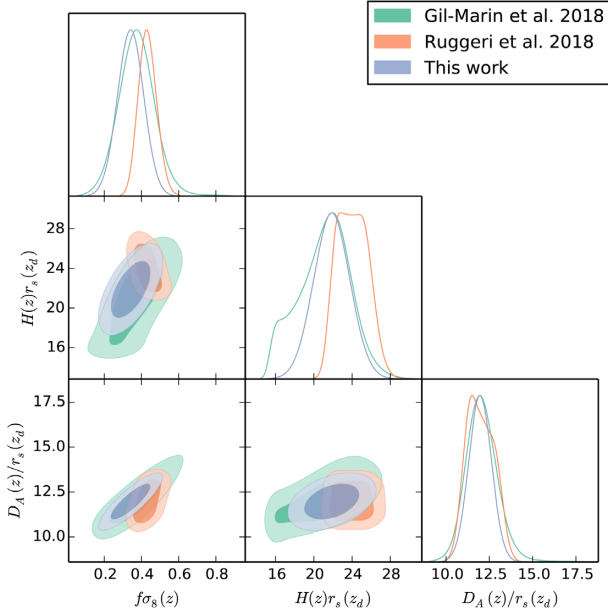
Figure 13. Constraints on $f\sigma_8$, D_A, and H, in comparison with another two analysis in Fourier space, Gil-Marín et al. (2018, green) and Ruggeri et al. (2018, orange). No redshift weights are applied in all the analysis shown in this plot.
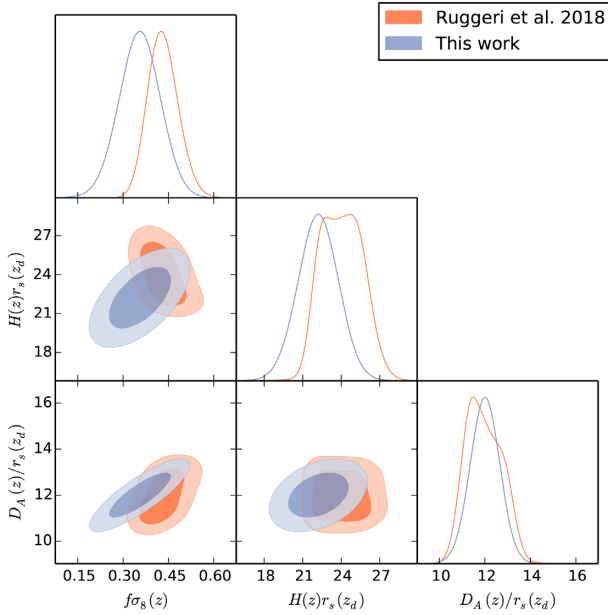
Figure 14. Constraints on $f\sigma_8$, D_A, and H, in comparison with another analysis in Fourier space, Ruggeri et al. (2018, orange). Redshift weights are applied in the analysis shown in this plot.

the Planck 2015 measurement by $\sim 1\sigma$, which is confirmed by an independent study in Fourier space in Gil-Marín et al. (2018) using the same galaxy catalogue. Gil-Marín et al. (2018) found that,

$$\{\Omega_M, \Omega_\Lambda\} = \left\{0.226^{+0.084}_{-0.093}, 0.55 \pm 0.14\right\} \quad (46)$$

using BAO measurements in three redshift slices (with effective redshifts of 1.19, 1.50, and 1.83) of the DR14Q sample. Given the level of uncertainty, we argue that this data combination is still consistent with the *Planck* observations, and the curvature of the

Universe is consistent with zero. However, we will re-investigate the consistency between quasar BAO and cosmic microwave background measurements when the final eBOSS quasar survey is completed.

Combining additional data sets, including the BOSS DR12 Lyman-α auto- and cross-correlation BAO measurements (Gontcho et al. 2018) and the isotropic BAO measurements using MGS (Ross et al. 2015) and 6dFGS (Beutler et al. 2011) samples, significantly improves the constraint, namely, a Universe without dark energy is excluded at 7.37σ by these BAO measurements, and the $\{\Omega_M, \Omega_\Lambda\}$ constraint using this full BAO data set is in excellent agreement with the Planck 2015 observations.

We then apply our joint BAO and RSD measurements to constrain the gravitational growth index γ together with Ω_M, and show the result in Fig. 16. Our measurement combined with BOSS DR12 consensus measurement yields $\gamma = 0.469 \pm 0.148$, which is consistent with the ΛCDM prediction of $\gamma \sim 0.545$. As shown in Table 5, this data combination prefers a low Ω_M, although the *Planck* measurement is still within the 68 per cent CL contour in Fig. 16.

Adding the *Planck* data tightens the constraint to $\gamma = 0.580 \pm 0.082$, which is consistent with the ΛCDM prediction. We overplot the 68 per cent CL uncertainty on γ and Ω_M derived from Gil-Marín et al. (2018) (the '3z' result) in Fig. 16 for a direct comparison. As shown, our constraint is in general agreement with that in Gil-Marín et al. (2018), although our constraint on γ is more stringent, probably due to the fact that our RSD measurement is tomographically more informative.

7 CONCLUSION AND DISCUSSIONS

We present a new and efficient method to extract the light-cone information for both RSD and BAO from galaxy redshift surveys, especially for those covering a wide redshift range.

Based on the optimal redshift weighting scheme, we measure the key parameters for BAO and RSD, namely, D_A, H, and $f\sigma_8$ for the eBOSS DR14Q sample at four effective redshifts of $z = 0.978$, 1.230, 1.526, and 1.944, and provide a full data covariance matrix (the key result of this work is presented in Tables 2 and 3). We find an excellent consistency between our measurement and those presented in companion papers, which analyse the same data set using different methods.

We apply our measurement to constrain the geometry of the Universe, and find that combining our BAO measurement with those from BOSS DR12, MGS, and 6dFGS, a Universe without dark energy is excluded at 7.4σ. Our RSD measurement combined with BOSS DR12 and *Planck* observations yield a constraint of the gravitational growth index, namely, $\gamma = 0.580 \pm 0.082$, which is fully consistent with the GR prediction.
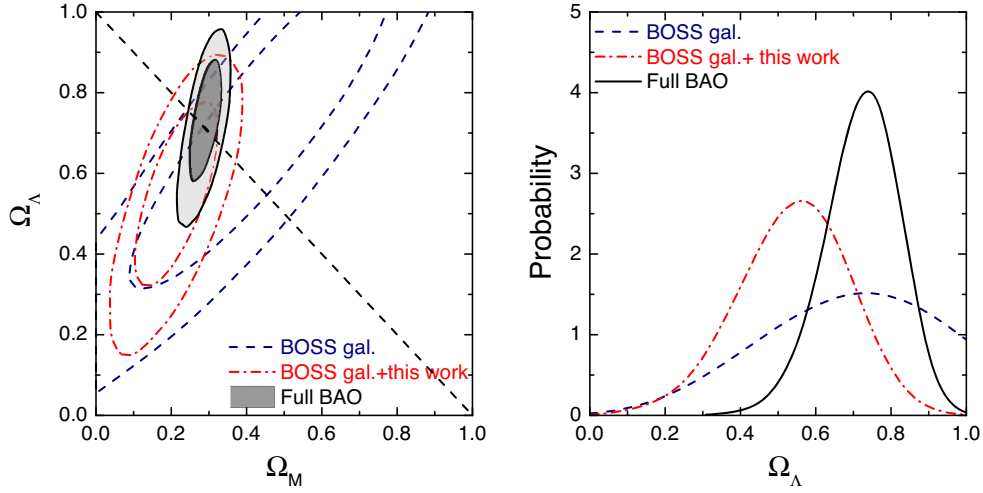
The method developed in this work can be used to extract the light-cone information from forthcoming deep redshift surveys including DESI,[8] PFS, [9] and *Euclid*,[10] which is crucial for cosmological studies of dark energy (Zhao et al. 2012, 2017a), neutrino mass, and modified gravity theories (Zhao et al. 2009a,b).

---

[8] http://desi.lbl.gov/
[9] http://pfs.ipmu.jp/
[10] https://www.euclid-ec.org/

Figure 15. Left: the 68 per cent and 95 per cent CL contours between Ω_M and Ω_Λ derived from different BAO data sets: BOSS gal. (the consensus BAO measurement in Alam et al. (2017); BOSS gal. + this work (the BOSS measurement combined with that in this work; Full BAO: BOSS gal. combined with this work and several additional BAO data sets including BOSS DR12 Lyman-α auto- and cross-correlation BAO measurements (Gontcho et al. 2018), and the isotropic BAO measurements using MGS (Ross et al. 2015) and 6dFGS (Beutler et al. 2011) samples; and right: the corresponding one-dimensional posterior distribution.

Table 5. The constraints on Ω_M, Ω_Λ, and $H_0 r_d$ (in unit of $km\,s^{-1}$) derived from three BAO data combinations. The signal-to-noise ratio of $\Omega_\Lambda > 0$ (S/N) and the FoM are also shown (the FoM of BOSS gal. is normalized to be unity for the ease of comparison).

	BOSS gal.	BOSS gal. + this work	Full BAO
Ω_M	0.443 ± 0.204	0.213 ± 0.070	0.289 ± 0.028
Ω_Λ	0.706 ± 0.239	0.540 ± 0.147	0.722 ± 0.098
$H_0 r_d$	9.820 ± 0.271	9.960 ± 0.253	10.166 ± 0.206
S/N	2.95	3.67	7.37
FoM	1	3.5	12.1
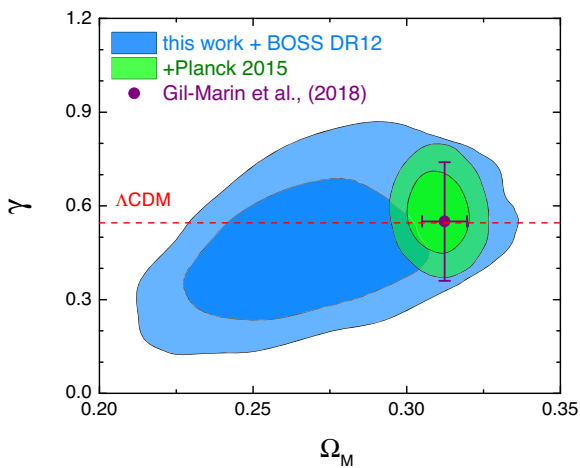
Figure 16. The 68 per cent and 95 per cent CL contour plots between Ω_M and γ derived from this work (presented in Tables 2 and 3) combined with the BOSS DR12 consensus result (blue), and with Planck 2015 combined (green). The data point with error bars shows the measurement from Gil-Marín et al. (2018). The horizontal dashed line shows the ΛCDM prediction, namely, $\gamma = 6/11$.

REFERENCES

Abolfathi B. et al., 2018, ApJS, 235, 42
Alam S. et al., 2017, MNRAS, 470, 2617
Alcock C., Paczynski B., 1979, Nature, 281, 358
Ata M. et al., 2018, MNRAS, 473, 4773
Baldauf T., Seljak U., Desjacques V., McDonald P., 2012, Phys. Rev. D, 86, 083540
Bautista J. E. et al., 2018, ApJ, 863, 110
Beutler F. et al., 2011, MNRAS, 416, 3017
Beutler F. et al., 2012, MNRAS, 423, 3430
Beutler F. et al., 2014, MNRAS, 443, 1065
Beutler F. et al., 2017, MNRAS, 466, 2242
Bianchi D., Gil-Marín H., Ruggeri R., Percival W. J., 2015, MNRAS, 453, L11
Blanton M. R. et al., 2017, AJ, 154, 28
Chan K. C., Scoccimarro R., 2012, Phys. Rev. D, 86, 103519
Chan K. C., Scoccimarro R., Sheth R. K., 2012, Phys. Rev. D, 85, 083509
Chuang C.-H., Kitaura F.-S., Prada F., Zhao C., Yepes G., 2015, MNRAS, 446, 2621
Contreras C. et al., 2013, MNRAS, 430, 924
Croom S. M. et al., 2005, MNRAS, 356, 415
Dawson K. S. et al., 2016, AJ, 151, 44
Eisenstein D. J. et al., 2005, ApJ, 633, 560
Eisenstein D. J. et al., 2011, AJ, 142, 72
Feldman H. A., Kaiser N., Peacock J. A., 1994, ApJ, 426, 23
Gil-Marín H. et al., 2018, MNRAS, 477, 1604
Gontcho S. G. A., Miralda-Escudé J., Font-Ribera A., Blomqvist M., Busca N. G., Rich J., 2018, MNRAS
Gunn J. E. et al., 2006, AJ, 131, 2332
Heavens A. F., Jimenez R., Lahav O., 2000, MNRAS, 317, 965
Hou J. et al., 2018, MNRAS
Howlett C., Percival W. J., 2017, MNRAS, 472, 4935
Kazin E. A. et al., 2014, MNRAS, 441, 3524
Koyama K., 2016, Rep. Prog. Phys., 79, 046902
Laurent P. et al., 2016, J. Cosmol. Astropart. Phys., 11, 060
Laurent P. et al., 2017, J. Cosmology Astropart. Phys., 7, 017
Lewis A., Bridle S., 2002, Phys. Rev., D66, 103511
Lewis A., Challinor A., Lasenby A., 2000, ApJ, 538, 473
Li J., Zhao G.-B., 2018, preprint (arXiv:1806.05022)
Linder E. V., 2005, Phys. Rev. D, 72, 043529
Myers A. D. et al., 2015, ApJS, 221, 27
O'Connell R., Eisenstein D. J., 2018, preprint (arXiv:1808.05978)
Pâris I. et al., 2017, A&A, 597, A79
Peacock J. A. et al., 2001, Nature, 410, 169
Percival W. J. et al., 2010, MNRAS, 401, 2148
Perlmutter S. et al., 1999, ApJ, 517, 565
Planck Collaboration et al., 2016, A&A, 594, A13
Riess A. G. et al., 1998, AJ, 116, 1009
Ross A. J., Samushia L., Howlett C., Percival W. J., Burden A., Manera M., 2015, MNRAS, 449, 835
Ross N. P. et al., 2009, ApJ, 697, 1634
Ruggeri R., Percival W. J., Gil-Marín H., Zhu F., Zhao G.-B., Wang Y., 2017, MNRAS, 464, 2698
Ruggeri R. et al., 2018, preprint (arXiv:1801.02891)
Saito S., Baldauf T., Vlah Z., Seljak U., Okumura T., McDonald P., 2014, Phys. Rev. D, 90, 123522
Samushia L. et al., 2014, MNRAS, 439, 3504
Scoccimarro R., 2004, Phys. Rev. D, 70, 083007
Seo H.-J., Eisenstein D. J., 2007, ApJ, 665, 14
Smee S. A. et al., 2013, AJ, 146, 32
Taruya A., Nishimichi T., Saito S., 2010, Phys. Rev. D, 82, 063522
Taruya A., Bernardeau F., Nishimichi T., Codis S., 2012, Phys. Rev. D, 86, 103528
Tegmark M., Taylor A. N., Heavens A. F., 1997, ApJ, 480, 22
The Dark Energy Survey Collaboration et al., 2017, preprint (arXiv:1712.06209)
Wang Y. et al., 2017, MNRAS, 469, 3762
Wang D. et al., 2018a, MNRAS, 477, 1528
Wang Y., Zhao G.-B., Chuang C.-H., Pellejero-Ibanez M., Zhao C., Kitaura F.-S., Rodriguez-Torres S., 2018b, MNRAS, 481, 3160
Weinberg D. H., Mortonson M. J., Eisenstein D. J., Hirata C., Riess A. G., Rozo E., 2013, Phys. Rep., 530, 87
Wilson M. J., Peacock J. A., Taylor A. N., de la Torre S., 2017, MNRAS, 464, 3121
Zarrouk P. et al., 2018, MNRAS, 477, 1639
Zhao G.-B., Pogosian L., Silvestri A., Zylberberg J., 2009a, Phys. Rev. D, 79, 083513
Zhao G.-B., Pogosian L., Silvestri A., Zylberberg J., 2009b, Phys. Rev. Lett., 103, 241301
Zhao G.-B., Crittenden R. G., Pogosian L., Zhang X., 2012, Phys. Rev. Lett., 109, 171301
Zhao G.-B. et al., 2016, MNRAS, 457, 2377
Zhao G.-B. et al., 2017a, Nat. Astron., 1, 627
Zhao G.-B. et al., 2017b, MNRAS, 466, 762
Zhu F., Padmanabhan N., White M., 2015, MNRAS, 451, 236
Zhu F., Padmanabhan N., White M., Ross A. J., Zhao G.-B., 2016, MNRAS, 461, 2867
Zhu F. et al., 2018, MNRAS, 480, 1096

APPENDIX A: THE PROCEDURE OF LINEARLY COMBINING THE CATALOGUES

In this section, we provide the procedure of linearly combining the redshift-weighted samples to yield one joint BAO and RSD measurement at a single effective redshift $z_{eff} = 1.526$, in order to compare with the measurement using the unweighted sample at the same effective redshift.
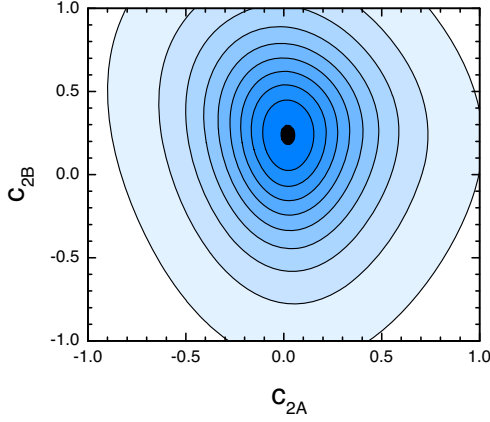
Figure A1. A contour plot of the c's for the redshift-weighted catalogues '2A' (with $z_{eff} = 0.98$) and '2B' (with $z_{eff} = 1.94$), and the colour shows the FoM defined in equation (A5). The contour lines from inside out illustrate the FoM from maximal to minimal values on linearly uniform intervals, and the black dot in the centre denotes the position where the FoM gets maximized.

(i) Suppose each of the four catalogues is assigned a coefficient c_i (i runs from 1 to 4), then the required effective redshift, which is 1.526 in our case, of the linearly combined sample is,

$$z_{eff} = \left(\sum_{i=1}^{4} c_i X_i \right) \bigg/ \left(\sum_{i=1}^{4} c_i Y_i \right), \tag{A1}$$

and Δ_2 defined in equation (44) of the combined sample can be calculated as,

$$\Delta_2 = \left(\sum_{i=1}^{4} c_i Z_i \right) \bigg/ \left(\sum_{i=1}^{4} c_i Y_i \right) - z_{eff}^2 \tag{A2}$$

where

$$X_i = \sum_j z_{i,j} w_{i,j}^2; \; Y_i = \sum_j w_{i,j}^2; \; Z_i = \sum_j z_{i,j}^2 w_{i,j}^2, \tag{A3}$$

here the index j runs over all the galaxies in the ith catalogue. Evaluate X, Y, and Z for each of the four catalogues using equation (A3);

(ii) Apply the constraint of

$$\sum_i c_i = 1, \tag{A4}$$

to properly normalize the linearly combined sample;

(iii) Compute the FoM of $\{D_A, H, f\sigma_8\}$ of the combined sample as,

$$\text{FoM} \equiv [\det(C_3)]^{-1/2} \tag{A5}$$

where C_3 is the 3×3 covariance matrix for $\{D_A, H, f\sigma_8\}$ for the combined sample, which can be derived by linearly combine the sixteen 3×3 submatrices, denoted as S, of C_{12}, the full 12×12 covariance matrix of the four samples, whose correlation matrix is shown in Fig. 10. Mathematically,

$$C_3 = \sum_{i,j} c_i c_j S_{i,j}. \tag{A6}$$

(iv) Equations (A1) and (A4) provide two constraints on the four γ's that we are after, then a maximization of the FoM defined in equation (A5) while keeping Δ_2 in equation (A2) negligible can in principle determine the c's.

This procedure finds that $c = \{0.02, 0.17, 0.57, 0.24\}$ for the weighted samples with $z_{eff} = 0.978, 1.230, 1.526$, and 1.944 respectively, and Fig. A1 shows a contour plot of the FoM as a function of the two coefficients.[11] Due to the correlation among the four catalogues, the trivial solution of $c = \{0, 0, 1, 0\}$ does not maximize the FoM.

APPENDIX B: THE PROCEDURE OF OBTAINING THE POSITIVE REDSHIFT WEIGHTS

In practice, we take the following procedures to find the positive-definite redshift weights, shown in the right-hand panels of Fig. 5, from the original weights, illustrated in the left-hand panels of Fig. 5.

(i) Take the SVD weights V_1 and V_2 for the monopole;
(ii) Rotate the V vectors by a linear transformation to obtain new weights W, namely,

$$W_1 = V_1 \cos\theta - V_2 \sin\theta + \lambda,$$
$$W_2 = V_1 \sin\theta + V_2 \cos\theta + \lambda,$$
$$W_3 = \lambda. \tag{B1}$$

where θ and λ are free parameters to ensure that,

(a) $W_i > 0$;
(b) The sum of dot products among the normalized W_i's gets minimized.

(iii) Repeat this process for the SVD weights for the quadrupole.

Note that we use the two-dimensional rotation matrix to transform the V vectors, which conserves the orthogonality of V. It is true that the additional shift by λ spoils the orthogonality, but this is kept to a minimal level because of the minimization procedure (ii).

APPENDIX C: THE MATLAB CODE FOR THE SVD ANALYSIS

We perform the SVD analysis using the following MATLAB code to find the orthogonal redshift weights shown in left-hand panels of Fig. 5, from the raw redshift weights shown in Fig. 3.

```
[m,n]  = size(w);
 percent Subtract off the mean of data
mn  = mean(w,2);
w   = w-repmat(mn,1,n);
 percent Construct the data matrix X
x   = w'/sqrt(n-1);
 percent SVD
[u,s,pc] = svd(x);
 percent Perform a projection
v   = pc'*w;
v   = v';
```

APPENDIX D: THE SURVEY WINDOW FUNCTIONS

The survey window functions for the four redshift-weighted samples are shown in Fig. D1. These window functions are derived following the method developed in Wilson et al. (2017).

---

[11] Note that only two of the coefficients are independent given the constraints equations (A1) and (A4).
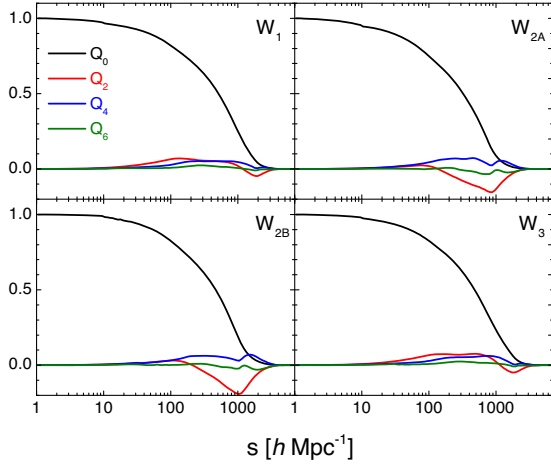
Figure D1. The window functions for four redshift-weighted samples, as shown in the legend.

[1]*National Astronomy Observatories, Chinese Academy of Sciences, Beijing 100012, P.R. China*

[2]*University of Chinese Academy of Sciences, Beijing 100049, China*

[3]*Institute of Cosmology & Gravitation, University of Portsmouth, Dennis Sciama Building, Portsmouth PO1 3FX, UK*

[4]*Max-Planck-Institut für Astrophysik, Karl-Schwarzschild-Str. 1, D-85741 Garching, Germany*

[5]*Sorbonne Universités, Institut Lagrange de Paris (ILP), 98 bis Boulevard Arago, F-75014 Paris, France*

[6]*Laboratoire de Physique Nucléaire et de Hautes Energies, Université Pierre et Marie Curie, 4 Place Jussieu, F-75005 Paris, France*

[7]*Leibniz-Institut für Astrophysik Potsdam (AIP), An der Sternwarte 16, D-14482 Potsdam, Germany*

[8]*Kavli Institute of Particle Astrophysics and Cosmology and Physics Department, Stanford University, Stanford, CA 94305, USA*

[9]*Department of Physics, Yale University, 260 Whitney Ave, New Haven, CT 06520, USA*

[10]*Center for Cosmology and Astro-Particle Physics, Ohio State University, Columbus, OH 43210, USA*

[11]*School of Physics and Astronomy, University of St Andrews, St Andrews, Scotland KY16 9SS, UK*

[12]*Aix-Marseille Université, CNRS, LAM (Laboratoire d'Astrophysique de Marseille), 38 rue F. Joliot-Curie, F-13388 Marseille Cedex 13, France*

[13]*Department of Physics and Astronomy, University of Wyoming, Laramie, WY 82071, USA*

[14]*Center for Cosmology and Particle Physics, Department of Physics, New York University, New York, NY 10003, USA*

[15]*IRFU,CEA, Université Paris-Saclay, F-91191 Gif-sur-Yvette, France*

[16]*Lawrence Berkeley National Lab, 1 Cyclotron Rd, Berkeley, CA 94720, USA*

[17]*Institut für Physik, Humboldt-Universität zu Berlin, Newtonstrasse 15, D-12589, Berlin, Germany*

[18]*Department Physics and Astronomy, University of Utah, 115 S 1400 E, Salt Lake City, UT 84112, USA*

[19]*Universitäts-Sternwarte München, Ludwig-Maximilians-Universität München, Scheinerstraße 1, D-81679 München, Germany*

[20]*Max-Planck-Institut für Extraterrestrische Physik, Postfach 1312, Giessenbachstr., D-85748 Garching bei München, Germany*

[21]*Instituto de Física, Universidad Nacional Autónoma de México, Apdo. Postal 20-364, México*

[22]*Department of Physics and Astronomy, Sejong University, Seoul 143-747, Korea*

[23]*Institute for Astronomy, University of Edinburgh, Royal Observatory, Blackford Hill, Edinburgh, UK*

[24]*Korea Astronomy and Space Science Institute, Yuseong-gu, 776 Daedeok daero, Daejeon 34055, Korea*

[25]*University of Science and Technology, Yuseong-gu 217 Gajeong-ro, Daejeon 34113, Korea*

[26]*Department of Astronomy and Astrophysics, The Pennsylvania State University, University Park, PA 16802, USA*

[27]*Institute for Gravitation and the Cosmos, The Pennsylvania State University, University Park, PA 16802, USA*

[28]*Tsinghua Center for Astrophysics and Department of Physics, Tsinghua University, Beijing 100084, China*

This paper has been typeset from a TEX/LATEX file prepared by the author.